

Picoperovskites: The Smallest Conceivable Isolated Halide Perovskite Structures Formed within Carbon Nanotubes

Reza J. Kashtiban,* Christopher E. Patrick, Quentin Ramasse, Richard I. Walton,* and Jeremy Sloan*

Halide perovskite structures are revolutionizing the design of optoelectronic materials, including solar cells, light-emitting diodes, and photovoltaics when formed at the quantum scale. Four isolated sub-nanometer, or picoscale, halide perovskite structures formed inside ≈ 1.2 – 1.6 nm single-walled carbon nanotubes (SWCNTs) by melt insertion from CsPbBr_3 and lead-free CsSnI_3 are reported. Three directly relate to the ABX_3 perovskite archetype while a fourth is a perovskite-like lamellar structure with alternating Cs_4 and polyhedral Sn_4I_x layers. In ≈ 1.4 nm-diameter SWCNTs, CsPbBr_3 forms $\text{Cs}_3\text{Pb}^{\text{I}}\text{Br}_5$ nanowires, one ABX_3 unit cell in cross section with the Pb^{2+} oxidation state maintained by ordered Cs^+ vacancies. Within ≈ 1.2 nm-diameter SWCNTs, CsPbBr_3 and CsSnI_3 form inorganic-polymer-like bilayer structures, one-fourth of an ABX_3 unit cell in cross section with systematically reproduced ABX_3 stoichiometry. Producing these smallest halide perovskite structures at their absolute synthetic cross-sectional limit enables quantum confinement effects with first-principles calculations demonstrating bandgap widening compared to corresponding bulk structural forms.

1. Introduction

The perovskite structure,^[1] with its almost infinitely adaptable array of derivatives, must count as one of the most important in materials science with the essential ABX_3 (A = a large cation; B = a smaller cation; X = an anion) structural archetype contributing to ferroelectric,^[2] piezoelectric,^[3] superconducting,^[4] photochemical,^[5] and many other technologically important properties. Interest in perovskites has recently been further accelerated by rapid developments in the fabrication of hybrid^[3,6–8] or all-inorganic halide perovskite ABX_3 ^[9,10] structures where A is an organic or alkali metal counterion, B typically lead or tin, and X a halogen, allowing materials with optical and photovoltaic characteristics^[11,12] exploitable in solar cells,^[13,14] ion-conducting materials,^[15] supercapacitors,^[16] and other energy storage devices^[17] to be developed. Bulk halide perovskites are however reactive, suffering from surface hydration,^[18] phase transformations,^[19,20] and high defect densities,^[21] reducing their performance and longevity. As a result, reduced-dimensionality halide perovskites focusing on colloidal,^[22] 2D,^[23] quantum dot,^[24] and, in thin films, molecular-scale^[25] preparations have been developed. While forming perovskites at such low dimension enhances some desirable characteristics, it can also increase their tendency to degrade, although surface passivation can reduce decomposition in thin films.^[26] Dimensionality is nonetheless key in engineering and fine tuning the physical properties of halide perovskites at the nanoscale due to its critical role in dictating electronic structure.^[27]

Here, we investigate steric stabilization of low-dimensional halide perovskites by encapsulating them within single walled carbon nanotubes (SWCNTs), graphene-derived structures^[28] that can increasingly be synthesized and refined with precise diameter and electronic selectivity.^[29] Encapsulating SWCNTs can regulate crystal growth at the atomic scale as a function of their internal diameter^[30] with single element or binary species as small as linear atom chains,^[31,32] atomic coils,^[33] twisting halide chains,^[30,32,34] and other molecular-scale species.^[35] In the context of this work, inorganic perovskites based on CsMX_3 (M = Pb^{2+} , Sn^{2+} ; X = Br, I) are desirable due to the likely ease of insertion from the melt^[30] and also taking into account also the respective imaging possibilities of these elements when

R. J. Kashtiban, J. Sloan
Department of Physics
University of Warwick
Coventry CV4 7AL, UK
E-mail: r.kashtiban@warwick.ac.uk; j.sloan@warwick.ac.uk

C. E. Patrick
Department of Materials
University of Oxford
Parks Road, Oxford OX1 3PH, UK

Q. Ramasse
SuperSTEM Laboratory
SciTech Daresbury Campus
Daresbury WA44AD, UK

Q. Ramasse
School of Chemical and Process Engineering
University of Leeds
Leeds LS2 9JT, UK

R. I. Walton
Department of Chemistry
University of Warwick
Coventry CV4 7AL, UK
E-mail: r.i.walton@warwick.ac.uk

 The ORCID identification number(s) for the author(s) of this article can be found under <https://doi.org/10.1002/adma.202208575>.

© 2023 The Authors. Advanced Materials published by Wiley-VCH GmbH. This is an open access article under the terms of the Creative Commons Attribution License, which permits use, distribution and reproduction in any medium, provided the original work is properly cited.

DOI: 10.1002/adma.202208575

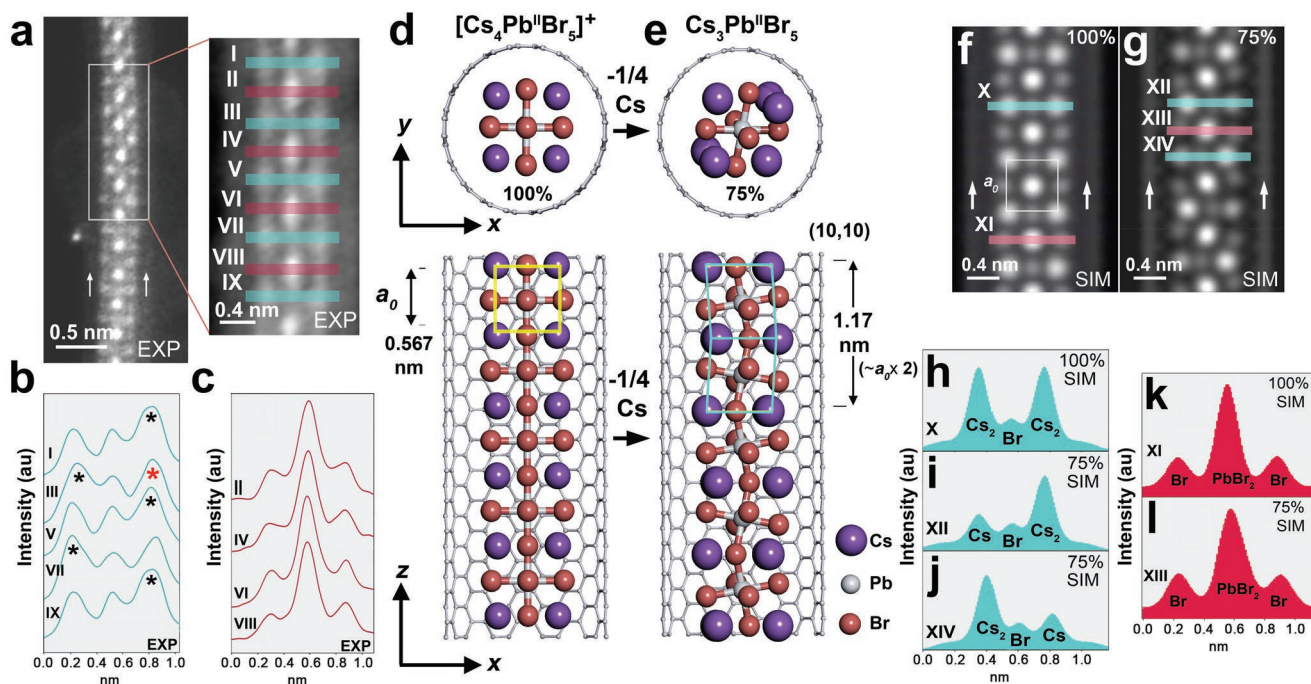


Figure 1. Encapsulated single-unit-cell wide $\text{Cs}_3\text{Pb}^{11}\text{Br}_5$ halide perovskite structure derived from CsPbBr_3 . a) HAADF image of $\text{Cs}_x\text{Pb}^y\text{Br}_z$ nanowire imaged inside a ≈ 1.4 nm SWCNT, walls indicated by arrows. Enlarged detail with 15 pixel wide regions indicated (I–X). b, c) Profiles I, III, V, VII, and IX from $\text{Cs}_x\text{--Br--Cs}_x$ ($x, x' = 1$ or 2) layers and II, IV, VI, and VIII from $\text{Br--PbBr}_2\text{--Br}$ layers. Alternating Cs_2 columns in $\text{Cs}_x\text{--Br--Cs}_x$ layers indicated by black asterisks with one excess Cs_2 column (red asterisk) indicated. d) DFT optimized $[\text{Cs}_4\text{Pb}^{11}\text{Br}_5]^+$ nanowire (100% Cs occupancy) in a (10,10) SWCNT viewed end-on and side-on with the ABX_3 unit cell overlaid. e) DFT optimized $\text{Cs}_3\text{Pb}^{11}\text{Br}_5$ nanowire (75% Cs occupancy) formed by removing one-fourth of Cs atoms. This lowest energy form (Figure S3a–c, Supporting Information) has alternating Cs_2 columns and systematic PbBr_6 octahedral tilting. f, g) TDS STEM simulations of optimized $[\text{Cs}_4\text{Pb}^{11}\text{Br}_5]^+$ and $\text{Cs}_3\text{Pb}^{11}\text{Br}_5$ structures. h, i) Simulated line profiles through $\text{Cs}_x\text{--Br--Cs}_x$ and $\text{Br--PbBr}_2\text{--Br}$ layers as indicated in (f) and (g).

imaged by high angle annular dark field (HAADF or ADF) scanning transmission electron microscopy (STEM). We use aberration corrected STEM together with atomically resolved electron energy loss spectroscopy (EELS) element mapping and high-resolution transmission electron microscopy (HRTEM) to investigate halide perovskite formation in 1.2–1.6 nm-diameter SWCNTs. First-principles density-functional theory (DFT) informed by the experimental data is then used to confirm the chemistry, investigate the stability of the imaged picoscale structures and provides insights into the formation of defects, structural conformation, and their individual electronic structures.

2. Results and Discussion

Following synthesis and prior to electron microscopy observation, both the CsPbBr_3 and CsSnI_3 bulk sample compositions were fully characterized by X-ray powder diffraction, scanning electron microscopy (SEM), and energy-dispersive X-ray microanalysis (EDX) in spot and linescan modes. After the SWCNTs were filled with CsPbBr_3 and CsSnI_3 , they were then analyzed again by local probe EDX analysis and EELS. Low magnification imaging by ADF STEM confirmed that at least 80–90% of all the observed SWCNTs in both cases were filled with CsPbBr_3 or CsSnI_3 . These preliminary analyses are presented in Figures S1–S6 (Supporting Information) and further infor-

mation is given in the Experimental Section and Supporting Information.

Figure 1a shows the first observation by HAADF of a $\text{Cs}_x\text{Pb}^y\text{Br}_z$ nanowire in an ≈ 1.4 nm-diameter SWCNT with two sets of line profiles (Figure 1b, c) through alternating $\text{Cs}_x\text{--Br--Cs}_x$ ($x, x' = 1, 2$) and $\text{Br--PbBr}_2\text{--Br}$ layers. A trial microstructure can be derived from a single $Pm\bar{3}m$ CsPbBr_3 unit cell extended along one lattice direction only (Figure 1d; Figure S7a–c, Supporting Information). If all possible Cs, Pb, and Br sites are occupied, this produces a net stoichiometry of $\text{Cs}_4\text{Pb}^1\text{Br}_5$ that is unfeasible due to a required +1 Pb oxidation state. In principle the SWCNT can also act as an electron donor or acceptor^[31,36] that could stabilize $[\text{Cs}_4\text{Pb}^1\text{Br}_5]^+$ formation but image intensity line profiles through successive $\text{Cs}_x\text{--Br--Cs}_x$ layers in the experimental image (Figure 1b) indicates that alternation occurs between Cs_2 and Cs atom columns within the nanowires. This reduces the average Cs occupancy to 75% from 100% and alters the stoichiometry to $\text{Cs}_3\text{Pb}^{11}\text{Br}_5$ with Pb in a more likely +2 oxidation state. Line profiles through interspersing $\text{Br--PbBr}_2\text{--Br}$ layers (Figure 1c) indicate that all atom positions in these layers are fully occupied, confirming the net composition as $\text{Cs}_3\text{Pb}^{11}\text{Br}_5$. Analysis of Cs_2/Cs alternation in $\text{Cs}_x\text{--Br--Cs}_x$ layers in an extended view of the same image (Figure S8a–d, Supporting Information) reveals some long-range variation in Cs versus Cs_2 occupancy and alternation but indicates an overall prevailing stoichiometry of $\approx \text{Cs}_{2.8}\text{PbBr}_5$.

To determine the lowest energy form of these structures, we performed DFT calculations on the 100% and 75% Cs occupied models to obtain the comparison structures in Figure 1d,e. The calculations employed plane waves and pseudopotentials, modelling exchange and correlation within a generalized-gradient approximation; full details are provided in the Methods section. The lowest energy form of the vacancy ordered $\text{Cs}_{4-x}\text{PbBr}_5$ model was found to be diagonally alternating Cs_2 and Cs columns with Cs vacancies maintained at the furthest distance (Figure S9a–c, Supporting Information). As discussed in Experimental Section, the DFT calculations were all performed for freestanding structures in vacuum, with test calculations that explicitly simulate the nanotube encapsulation yielding very similar structures. These models were then used to produce STEM simulated images in Figure 1f,g that incorporate thermal diffuse scattering (TDS) by the frozen phonon method^[37] (i.e., TDS STEM simulations, Table S1, Supporting Information^[38,39]). Comparison between fully occupied $\text{Cs}_2\text{--Br--Cs}_2$ line profiles (Figure 1h) with simulated alternating Cs_2 occupancy $\text{Cs}_x\text{--Br--Cs}_x$ line profiles (Figure 1i,j) reveals that the latter more accurately reproduces the observed image contrast in Figure 1a,c. A closer comparison of DFT optimized $[\text{Cs}_x\text{Pb}^{II}\text{Br}_5]^+$ and $\text{Cs}_3\text{Pb}^{II}\text{Br}_5$ models in Figure 1d,e reveals distortions in both the Cs and Br substructures, more visible in a second lower background image and reproduced in corresponding TDS STEM simulations (Figure S9d,f, Sup-

porting Information). These observed distortions are comparable to those that cause the symmetry lowering of cubic $Pm\bar{3}m$ CsPbBr_3 to orthorhombic $Pbnm$ CsPbBr_3 ^[38] that occurs due to octahedral tilting and rotation (Figure S9g,h, Supporting Information). While bulk and nanoscale distortions observed in bulk CsPbBr_3 and nanowire $\text{Cs}_3\text{Pb}^{II}\text{Br}_5$ have different origins, it is particularly significant that these are observable at the nanoscale due to their role in influencing electronic properties.^[24,27] What is also significant is that, in our $\text{Cs}_3\text{Pb}^{II}\text{Br}_5$ nanowires, we observe systematically ordered vacancies required to maintain Pb^{2+} in a charge balanced structure. These are therefore not “introduced” vacancies, as in for example theoretical studies on $\text{Cs}_{1-x}\text{SnBr}_3$,^[40] but instead are a natural consequence of the need of a perovskite structure to maintain charge balance under extreme steric confinement.

A second structure type observed in narrower ≈ 1.2 nm-diameter SWCNTs is shown in Figure 2 consisting of encapsulated bilayer $\text{CsPb}^{II}\text{Br}_3$ crystals. Raw and Wien-filtered experimental ADF-STEM images (Figure 2a,b) show a structure in which alternating layers are imaged either as short, blurred segments or pairs of discrete spots (Figure 2b). Longitudinal profiles I and II (Figure 2b,c) reveal an average periodicity of ≈ 0.58 nm, consistent with two PbBr_2 layer separations, whereas cross-sectional line profiles III and IV (Figure 2b,d) indicate blurred imaged PbBr_2 layers (denoted B) alternating with a layer consisting of Cs and Pb atom columns. Owing

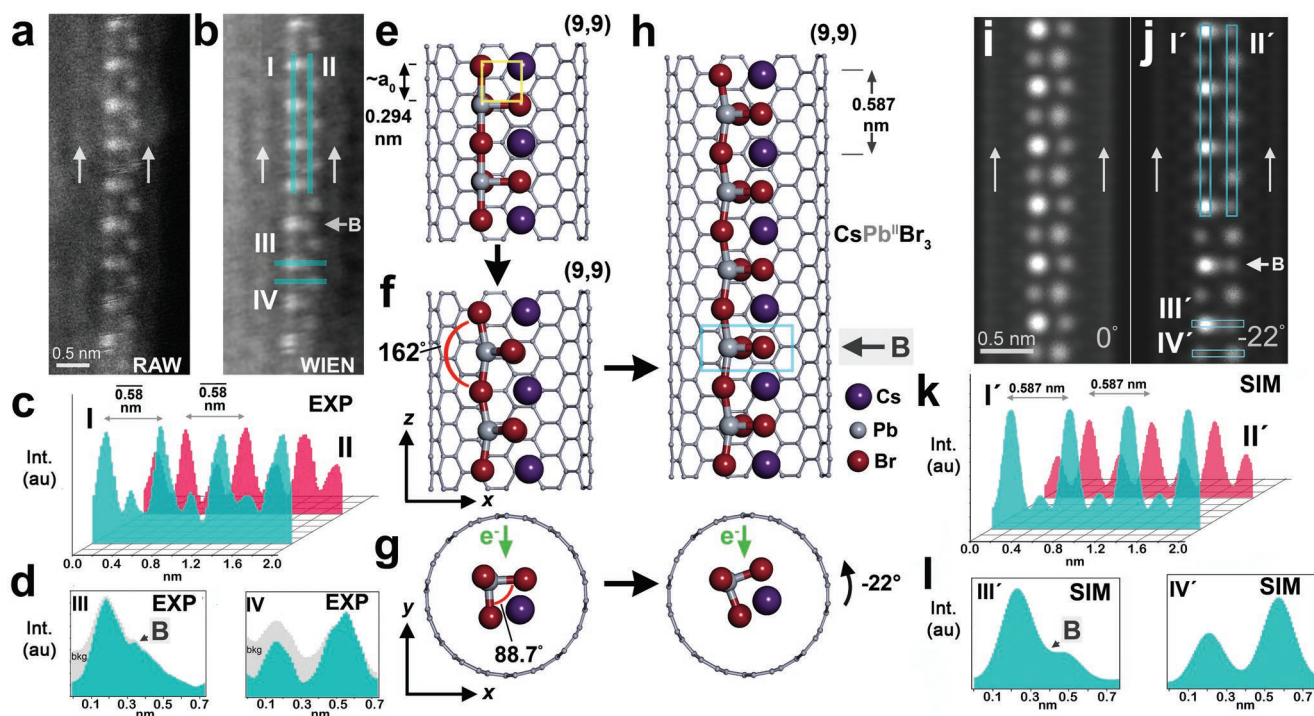


Figure 2. Encapsulated bilayer $\text{CsPb}^{II}\text{Br}_3$ perovskite-like structure derived from $Pm\bar{3}m$ CsPbBr_3 . a,b) Raw unfiltered and Wien filtered experimental images of polymeric $\text{CsPb}^{II}\text{Br}_3$ bilayer structure with 10 pixel wide profiles I, II, III, and IV indicated. c,d) Longitudinal profiles I and II and cross-sectional III, IV profiles as indicated in (b). e) Side view of unoptimized $\text{CsPb}^{II}\text{Br}_3$ bilayer structure derived from a partial $Pm\bar{3}m$ CsPbBr_3 unit cell (Figure S7d,e, Supporting Information) in a (9,9) SWCNT. f,g) DFT optimization of structure in (b) in the same relative orientation with added end-on view. h) extended model of the structure in (f) and (g) but in which the CsPbBr_3 nanowire is rotated -22° relative to g). i,j) TDS STEM simulations of DFT optimized $\text{CsPb}^{II}\text{Br}_3$ bilayer structures in the two orientations as indicated in g) and h). k,l) longitudinal and cross-sectional line profiles (I'–IV') through the TDS STEM simulations as indicated in (j). The green arrows in (g) and (h) indicate electron beam direction.

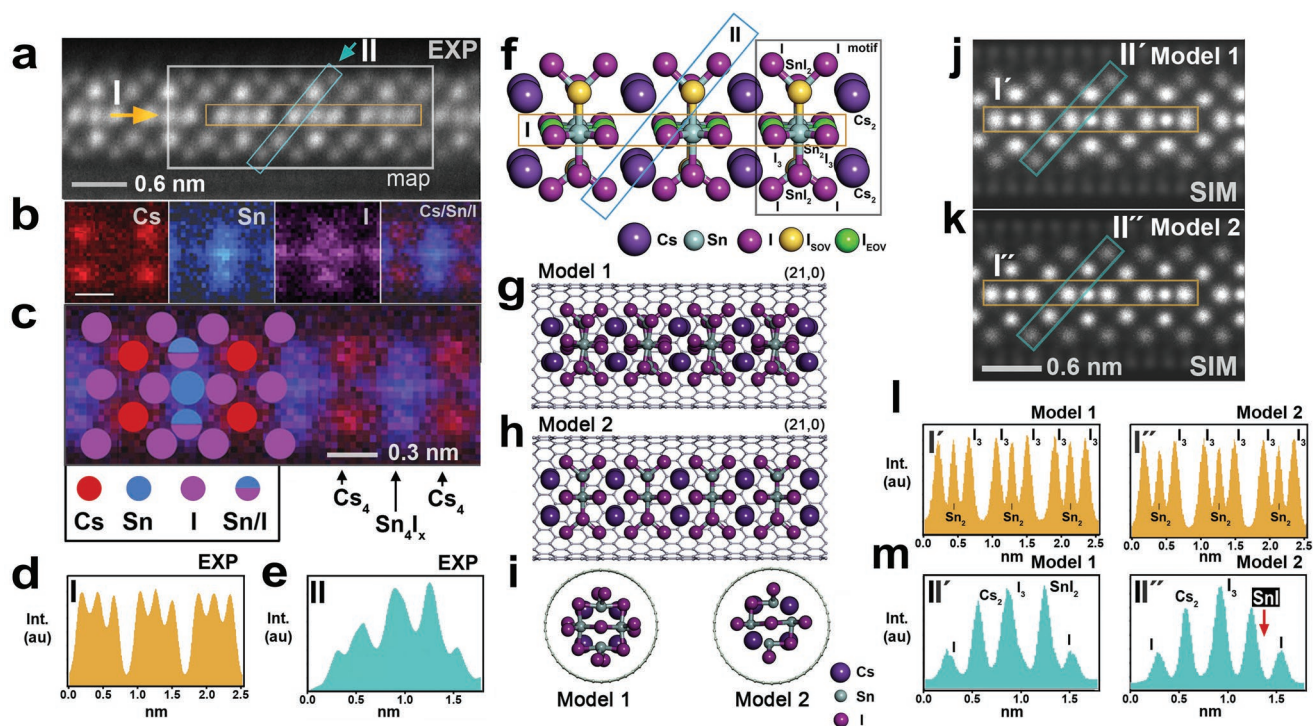


Figure 3. Lamellar perovskite derivative in a ≈ 1.6 nm-diameter SWCNT. a) 60 kV HAADF image of novel lamellar encapsulated cesium tin iodide structure with longitudinal and diagonal profiles I and II indicated. b) Cs, Sn, I and Cs/Sn/I EELS element maps obtained from the “map” region in (a). c) Cs/Sn/I EELS map with overlaid motif added. d,e) Experimental line profiles I and II. f) General structure motif with locations of surface (I_{SOV}) and equatorial iodine vacancies (I_{EOV}) in Models 2–3 indicated. g) Optimized Model 1 with all I positions in (f) occupied to give $[Cs_4Sn_4I_{14}]^{2-}$. h) Optimized Model 2 with vacancies created by removing I from the indicated I_{SOV} positions in (f) to give $Cs_4Sn_4I_{12}$. Model 3, with vacancies created at the I_{EOV} positions in (f) appears in Figure S10 (Supporting Information) with extended simulations of Models 1 and 2. j,k) TDS ADF-STEM simulations of Models 1 and 2. l,m) longitudinal (I' and I'') and diagonal (II' and II'') line profiles as indicated in (j) and (k) with atom columns indicated. Each $I-Cs_2-I_3-SnI_2-I$ (or $I-Cs_2-I_3-SnI-I$) layer has a complementary adjacent layer with Cs_2 and SnI_2 (or SnI) columns switched. Note reduction in SnI column profile (arrowed).

to systematic coordination reduction imposed by confinement, this bilayer structure recreates the ABX_3 stoichiometry as $CsPb^{II}Br_3$ with Pb in +2 oxidation state. A trial model of bilayer $CsPb^{II}Br_3$ (Figure 2e) derived from one-fourth of a unit cell of $Pm\bar{3}m$ $CsPbBr_3$ in cross section (Figure S1d,e, Supporting Information) was used as the basis for the DFT optimized model in Figure 2f,g. In Figure 2e, all $Br-Pb-Br$ internal angles are 90° but, following optimization, longitudinal $Br-Pb-Br$ angles relax to $\approx 162^\circ$ (Figure 2e) and cross-sectional $Br-Pb-Br$ angles to $\approx 88.7^\circ$ (Figure 2g). To recreate the diffuse features in Figure 1a,b it was necessary to rotate the optimized model as indicated in Figure 2h, to allow staggering of the atoms in the $PbBr_2$ layers in the electron beam direction (green arrow Figure 2g,h) precisely recreating the observed blurring (B, Figure 1b,d). TDS STEM simulations produced from unstaggered versus staggered bilayer $CsPb^{II}Br_3$ models (Figure 2i,j) show that only the latter reproduces the blurring observed in both the experimental images and corresponding line profiles (Figure 2d,l). This sub-unit-cell form is unprecedented but clearly retains a structural lineage and stoichiometric relationship with the parent $Pm\bar{3}m$ $CsPbBr_3$ perovskite structure, as shown in Figure S7d,e (Supporting Information). This 1D structure demonstrates what happens when ABX_3 perovskite is “edited” by confinement to two atomic layers in cross-section creating also a carbon free $[-PbBr_3]_x$ chain that also conforms to the standard definition of an inorganic polymer.^[41]

In addition to the cesium lead bromide structures, we also encapsulated lead-free cesium tin iodide compositions. In Figure 3, we present a novel structure, imaged inside ≈ 1.6 nm-diameter SWCNTs by HAADF, consisting of Cs_4 layers interspersed with Sn_4I_x layers, morphologically similar to lamellar perovskite-like phases such as $CsPb_2Br_5$.^[42] Element-selective atomically resolved EELS produces Cs, Sn, I, and Cs/Sn/I $M_{4,5}$ element maps (Figure 3b,c) which, in combination with STEM line profiles (Figure 3d,e), allow us to construct a general motif, initially with full iodine occupancy (Figure 3f). This motif was used to construct trial models for DFT optimization (Figure 3g,i) and TDS STEM simulations (Figure 3j,k). If all iodine positions in Figure 3f are occupied, this creates $[Cs_4Sn_4I_{14}]^{2-}$ that optimizes to produce Model 1 (Figure 3g,i), simulated in Figure 3j. If alternating surface iodine vacancies (i.e., I_{SOV}) are created in the motif in Figure 3f, this produces $Cs_4Sn_4I_{12}$ that optimizes to create Model 2 (Figure 3g,i), simulated in Figure 3k. We also investigated Model 3 in which all the equatorial iodines are removed from the motif in Figure 3f, creating ordered equatorial iodine vacancies (i.e., I_{EOV}), which also creates $Cs_4Sn_4I_{12}$ stoichiometry but this form does not optimize into a regular structure. All three models are compared in Figure S10 (Supporting Information).

In terms of structural verification, line profiles I and II through HAADF images (Figure 3a,d,e) provide the best

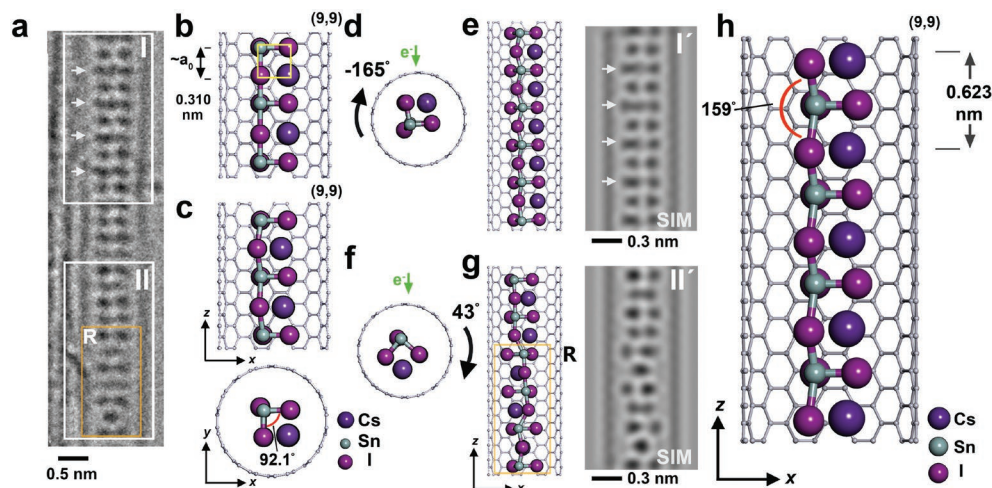


Figure 4. Encapsulated bilayer CsSnI_3 -perovskite-like polymeric structure derived from $Pm\bar{3}m$ CsSnI_3 . a) HRTEM image of CsSnI_3 bilayer structure with ordered region I with blurred SnI_2 layers (arrowed) alternating with Cs/I single atom columns. A rotated region R appears in section II. b) Unoptimized bilayer structure derived from a partial $Pm\bar{3}m$ CsSnI_3 cell grown along one lattice direction in a (9,9) SWCNT (Figure S11, Supporting Information). c) As (b) following DFT optimization, end-on view at bottom. d) As (c) but rotated -165° as indicated and corresponding simulation (cf. section I in (a)). Blurs in rotated SnI_2 layers produced by Sn/I staggering are arrowed. f,g) As (c) but with local 43° rotation of section R relative to (c) and corresponding simulation. h) Enlarged view of DFT-optimized CsSnI_3 bilayer structure with calculated repeat and longitudinal I–Sn–I angle indicated. The green arrows in (d) and (e) indicate electron beam direction.

experimental data for comparison with the TDS STEM simulations (Figure 3j,k; Figure S10, Supporting Information) produced from the optimized “best match” Models 1 and 2 (Figure 3g–i). For the extended simulations (Figure S10, Supporting Information), we use low or high I phonon values with typical Cs and Sn values (Table S1, Supporting Information). The closest matches in Figure 2j,k were produced using the high I phonon value. Equatorial profiles I' or I'' correspond to $\text{I}_3\text{--Sn}_2\text{--I}_3$ (Figure 3l) whereas, for Model 1, diagonal profile II' corresponds to $\text{I--Cs}_2\text{--I}_3\text{--SnI}_2\text{--I}$ and, for Model 2, profile II'' corresponds to $\text{I--Cs}_2\text{--I}_3\text{--SnI--I}$ (Figure 3m) with reduced scattering from SnI columns arrowed. The fully occupied Model I ($[\text{Cs}_4\text{Sn}_4\text{I}_{14}]^{2-}$) simulation in Figure 3j most accurately reproduces the experimentally imaged structure in Figure 3a. Because of distortion during relaxation, Model 3 simulations (with I_{EOV} vacancies) do not produce a good match (Figure S10, Supporting Information).

The final structure we report here is a bilayer CsSnI_3 structure isostructural to bilayer CsPbI_3 (Figure 2a–l) that we have imaged by HRTEM (Figure 4a). In common with the latter, the microstructure consists of staggered SnI_2 layers alternating with Cs and I single atom column layers as depicted in Figure 4b and by the DFT optimized model in Figure 4c. As with bilayer CsPbBr_3 , it is also necessary to rotate the crystal by some angle (Figure 4c,d) to reproduce the observed blurring in SnI_2 layers by HRTEM multislice simulation (Figure 4f). This structure has locally rotated domains (denoted II in Figure 4) and appears less rigid than bilayer CsPbI_3 . To simulate this region, we rotate and then simulate a subregion of this crystal (R) as indicated in Figure 4f,g. As with bilayer CsPbI_3 , optimal CsSnI_3 stoichiometry is systematically returned by confinement. In the optimized structure (Figure 4h), in plane I–Sn–I bonds relax to $\approx 159^\circ$ and cross-sectional I–Sn–I angles distort to $\approx 92.1^\circ$. This is a second example of an isolated sub-

unit-cell perovskite structure that also can be described as an inorganic polymer.^[41]

Our DFT calculations further detail the role that the nanotube diameter plays in influencing electronic structure and nanowire stability. Band structures and partial densities of states (PDOS) calculated within a generalized gradient approximation (Perdew–Burke–Ernzerhof, PBE) to exchange and correlation (Experimental Section, Figure 5; Figure S12, Supporting Information) confirm all four structures are semiconducting. The structures have the same orbital characteristics as bulk CsPbBr_3 and CsSnI_3 with antibonding Bs/Xp ($\text{B} = \text{Sn}, \text{Pb}; \text{X} = \text{Br}, \text{I}$) in the valence band and Bp/Xp in the conduction band.^[43,44] The Cs atoms do not contribute states to the conduction and valence bands, so there are no discernible features associated with the Cs vacancies in $\text{Cs}_3\text{PbI}_3\text{Br}_5$. Calculated bandgaps, typically underestimated by DFT-PBE, are all of the order of 2 eV when spin–orbit effects are included, significantly larger than values calculated for the bulk CsPbBr_3 and CsSnI_3 (0.56 and 0.07 eV, respectively). Repeating these calculations in a hybrid description of exchange (PBE0) finds a similar opening of the gap, between 1.4 and 1.8 eV (Figure S13 and Table S5, Supporting Information).

This opening of the bandgap is a striking illustration of quantum confinement, with the reduced dimensionality of the 1D structures leading to an increased bandgap. It is interesting to place our findings in the context of wider investigations of quantum confinement for low-dimensional perovskites^[45,46] and other systems.^[47] Models employed in refs. [45] and [46] predict the opening of the bandgap to be inversely proportional to the square of the size of the material along the confined direction(s) d and also inversely proportional to a coefficient k which is 1 for a quantum dot, 2 for a slab, and 1.71 for a wire, comparable to results reported for InP quantum wires.^[47] According to ref. [45], the expected gap opening of a 0.5 nm-thick slab of

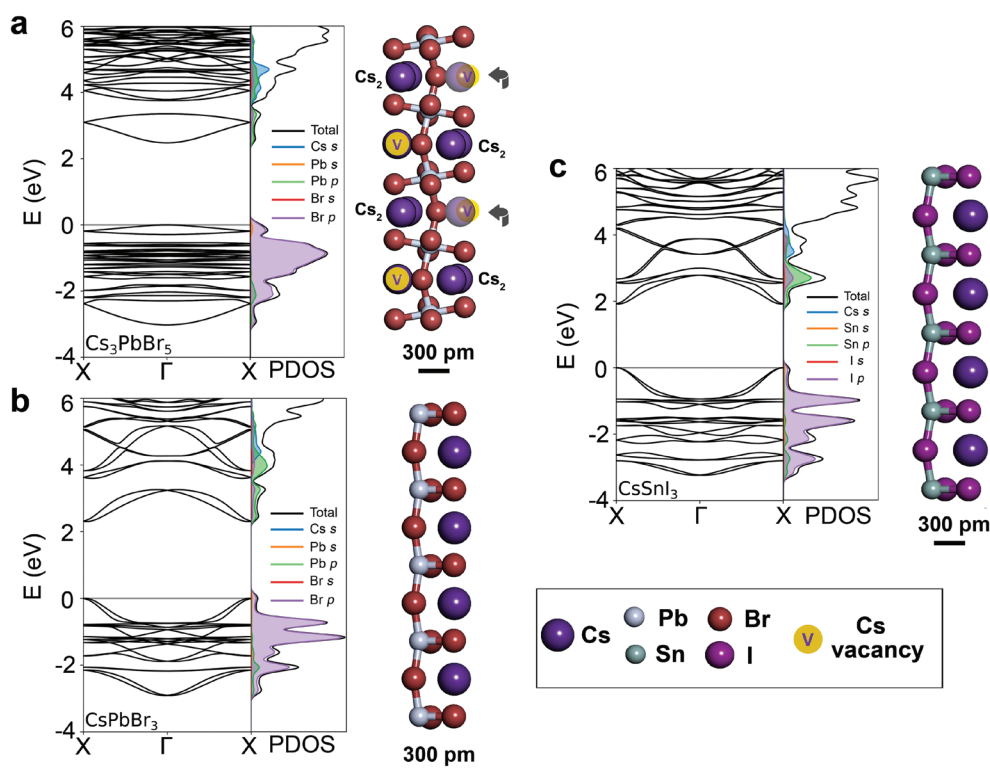


Figure 5. Electronic structure and models of Cs_3PbBr_5 , CsPbBr_3 , and CsSnI_3 picoperovskites (pm scale added). All band structures and PDOS are calculated at the PBE level of theory, with spin–orbit effects included through the use of relativistic pseudopotentials. a) The calculated band structure of Cs_3PbBr_5 is for the most highly optimized form of the 75% Cs occupied structure with distances between Cs vacancies maximised (Figure 1e) as indicated in the structure at right (see also Figure S9, Supporting Information). The determined bandgap is 2.25 eV. b) Calculated band structure for the CsPbBr_3 encapsulated bilayer structure (Figure 2h). The determined bandgap is 2.31 eV. c) Calculated band structure for the CsSnI_3 encapsulated bilayer structure (Figure 4h). The determined bandgap is 1.92 eV. Further details about these calculations and structures are given in the Supporting Information and in Tables S1–S3 (Supporting Information).

CsPbBr_3 is 0.9 eV. The dimensions of our wires range from 0.3 to 0.6 nm (Figures 1–4), so applying this model here predicts gap openings of 0.7–2.9 eV depending on the value used for d , consistent with our calculations.

We have also investigated a second model based on the tight-binding approach, where we consider a simple cubic lattice of atoms, spacing a , with two non-hybridizing orbitals per atom which are well separated in energy by an amount E_0 . Assuming only nearest-neighbor interactions with a bonding integral of t gives the following expressions for the conduction and valence bands, respectively:

$$E_c(k) = E_0 + 2t[\cos(k_x a) + \cos(k_y a) + \cos(k_z a)] \quad (1)$$

$$E_v(k) = -2t[\cos(k_x a) + \cos(k_y a) + \cos(k_z a)] \quad (2)$$

Choosing the parameters E_0 and t as 3.6 and 0.15 eV, this highly simplified model can account for the gross features of the DFT-PBE dispersions of the conduction and valence bands, particularly the gaps at the high-symmetry points of the Brillouin zone (Figure S14; note these calculations do not include spin–orbit coupling). If we now take the same model and parameters but restrict the electron motion to one dimension, the gap opens by an amount $8t$, i.e., 1.2 eV, which matches

well the DFT-PBE gap opening (Table S5). Therefore, two simple, but very different, models of quantum confinement yield results which are consistent with our explicit calculations.

The band structures in Figure 5 and S12 show dispersion along the nanotube axes indicating that electrons remain mobile in this direction. For the lamellar nanowire in a ≈ 1.6 nm SWCNT in Figure 3, it is notable that the ground state energy of $\text{Cs}_4\text{Sn}_4\text{I}_{12}$ with surface ordered vacancies (Model 2) is lower in formation energy than bilayer CsSnI_3 by 175 meV per ABX_3 equivalent (Table S3, Supporting Information). Formation of bilayer polymeric CsSnI_3 is favored only when the nanotube diameter is sufficiently small ($> \approx 1.2$ nm) to prevent the formation of larger uncharged lamellar structures. On the other hand, the formation of charged $[\text{Cs}_4\text{Sn}_4\text{I}_{14}]^{2-}$ (Model 1), favored by our imaging studies, can also possibly be stabilized by SWCNT charge accommodation^[31,36,48] rather than by steric stabilization as in bilayer CsPbI_3 and CsSnI_3 . In terms of the electronic structure of Models 1 and 2, the excess iodine in Model 1 would have the effect of hole-doping the structure. Introducing the 2– charge compensates this effect and leads to a filled valence band. Interestingly, removal of iodine in model 2 leads to a relatively flat band below the main conduction manifold (Figure S12, Supporting Information) that likely represents a localized defect state. Further work should focus on characterizing the optoelectronic properties of these materials and this state in particular.

3. Conclusion

Our studies show that we can systematically create new generations of halide perovskite structures by sterically stabilizing them inside variable diameter SWCNTs. Another important aspect of these studies is how halide perovskite surface chemistry responds to confinement that will impact profoundly on their structural and physical properties as seen in surface studies of lattice terminated perovskites. Surface states in terminated halide perovskites reconstruct according to a variety of mechanisms revealed by scanning tunneling microscopy, enabling halide dimers or “zig-zag” patterns to be imaged.^[49] While we image perovskites formed by confinement, we nonetheless see the surface structural consequences. In the case of 75% occupied Cs₃PbBr₅, ordered Cs vacancies induce tilting in the local structure, features which are known to influence optoelectronic properties^[40] and charge carrier mobility.^[50,51] Another likely consequence, similar to the investigations described in ref. [31], is the impact of lamellar charge variant structures in SWCNTs. The previous study showed that linear chains of Cs⁺ and I⁻ ions cause the external electronic structures of narrow SWCNTs to fluctuate. We should expect similar charge modification in wider nanotubes from the lamellar structures described in Figure 3.

The extensive literature of carbon nanotubes, perovskites, and halide perovskites will provide further pathways to modification and exploitation. The SWCNTs can themselves be chirally refined^[29] to produce tubules with unique electronic structures^[52] and a single (*n,m*) chirality will also selectively produce each individual encapsulated structure described here in a pure composite form. Encapsulating nanotubes can also be produced from other materials including insulating boron nitride (BN)^[53] or semiconducting dichalcogenides (MoS₂, WS₂, etc.).^[54,55] At a more fundamental level, the nanowire band structures (Figure 5; Figure S12, Supporting Information) could be tuned by chemical substitution^[56] or doping.^[57] These various possibilities provide road maps for targeted synthesis of specific 1D perovskite structures, allowing a new generation of low-dimensional halide perovskite structures to be designed and synthesized beyond this preliminary work. The nature of the crystal growth we observe indicates a dominant relationship between the confining nanotube diameter, its internal surface, and the obtained crystal structure enabling us, in the limit, to see halide perovskites formed at the polymeric scale for the first time.

4. Experimental Section

Preparation of CsPbBr₃ and CsSnI₃ Filled SWCNTs for Electron Microscopy: CsPbBr₃ and CsSnI₃ were prepared by solid-state synthesis using mixtures of CsBr and PbBr₂ or CsI and SnI₂, respectively. All precursors were sourced from Merck in their maximum available purity (99.999%) and stoichiometric mixtures of the bromide and iodide compositions were finely ground using an agate mortar and pestle inside an argon-atmosphere glove box. Each mixture was transferred into 10 cm silica quartz ampoule that were sealed under vacuum (10⁻³ Torr) using an oxygen–methane torch. The sealed ampoules were transferred into a muffle furnace, heated at 2 °C min⁻¹ to 480 °C and held for 5 h and cooled to room temperature at 1 °C min⁻¹. The as prepared CsPbBr₃ and CsSnI₃ were deposited inside SWCNTs, supplied by NanoIntegris, with a specified diameter range of 1.2–1.7 nm according

to a published melt protocol.^[58] Two quantities of 20 mg of SWCNTs were oxidized in open air at 480 °C before being intimately mixed in a mortar and pestle with separate 10 mg quantities of CsSnI₃ and CsPbBr₃ before being placed separately in 10 cm ampoules sealed under vacuum (10⁻³ Torr). The CsPbBr₃ and CsSnI₃ SWCNT mixtures were then heated to 555 °C and 480 °C for 12 h dwell periods respectively employing ramp rates of 2 °C min⁻¹ and cooling rates of 1 °C min. Each sample was then ultrasonically dispersed in ethanol before drop casting onto 3.05 mm lacey carbon coated copper grids (Agar) for examination by electron microscopy.

Powder X-ray Diffraction: Powder X-ray diffraction (XRD) was measured from polycrystalline powders of CsPbBr₃ and CsSnI₃ using one of two diffractometers. A Rigaku SuperNova diffractometer with microfocus Mo tube giving Kα_{1/2} radiation was used to study a small amount of the powdered sample mounted on a Mitegen cryomount with Foblin oil to protect the sample from air. An Atlas S2 CCD detector was used in 1×1 binning that gave slightly sharper peaks and also better data at the lower angles. The sample was spun to give better counting statistics. The instrument had been previously calibrated using 2-dimethylsulfuranylideneindan-1,3-dione standard at two different distances. Alternatively, a third Generation Malvern Panalytical Empyrean equipped with multicore (iCore/dCore) optics giving Cu Kα_{1/2} radiation was used. A Pixel 3D detector was used on the diffracted beam optics. The samples were mounted in an Anton Paar dome sample holder under nitrogen with a PEEK dome and zero-background insert. Simulated diffraction patterns were calculated using the program Mercury 3.1 using crystallographic information files from the Inorganic Crystal Structure Database (ICSD) produced from published crystal structures.^[24,39]

Electron Microscopy Imaging and Simulation: Scanning electron microscopy was performed using a ZEISS SUPRA 55-VP FEGSEM scanning electron microscope (Oberkochen, Germany) using a field emission gun with an accelerating voltage between 5 and 20 kV and fitted with an Oxford Instruments (Abingdon, UK) energy-dispersive X-ray spectroscopy (EDS) spectrometer that allows elemental composition analysis. A double-corrected JEM-ARM 200F microscope operating at 80 kV equipped with CEOS imaging aberration and probe correction and a Gatan SC1000 ORIUS camera with a 4008×2672 pixel CCD was used for HRTEM and ADF STEM investigations. ADF STEM images were obtained with a JEOL annular field detector with a fine imaging probe with a convergence semi-angle of a ≈25 mrad, a probe current of ≈23 pA and an inner angle of 45–50 mrad. Elemental mapping and EDX line scans were collected on an Oxford Instruments 100 mm² windowless detector to examine the distribution of elements in selected materials. Line scan data were normalized for each element under investigation. HAADF imaging and electron energy loss spectroscopy (EELS) were also carried out in a Nion UltraSTEM100 equipped with a Gatan Enfina spectrometer. This instrument was operated at 60 kV acceleration voltage to minimise knock-on damage to the SWCNTs, and the STEM probe forming optics were adjusted to provide a 20 pA beam with a ≈33 mrad convergence angle—resulting in an estimated probe size of ≈0.1 nm. The EEL spectrometer entrance aperture half-angle acceptance was 36 mrad, while the HAADF detector inner and outer angles were 85 and 190 mrad, respectively. Chemical maps were produced from acquired EELS data by integrating the intensity of the relevant ionisation edges (Cs, Sn, Pb, Br, and I *M*_{4,5}) over a 75 eV window above their respective onsets, after subtraction of the decaying background using a standard power law Model. A spectral dispersion of 0.5 eV per channel was used to capture both edges simultaneously (resulting in a point-spread limited effective energy resolution of ≈1 eV); to further boost signal-to-noise the data were binned (×2) spectrally prior to generating the EELS maps, but no statistical denoising was applied.

HAADF, ADF, and HRTEM Simulation: Electron microscopy simulation in STEM and HRTEM modes ADF STEM simulations were performed using cITEM 0.3.3a, an open-source GPU accelerated multislice program.^[59] Simulation parameters were matched to the microscope aberrations as measured by the CEOS control software and also duplicating the imaging conditions stated above for either the ARM200F electron microscope operating in STEM mode at 80 kV

or the Nion UltraSTEM100 dedicated STEM operated at 60 kV. Thermal diffuse scattering was modeled using the frozen phonon method with at least 30 iterations per simulation and using the representative phonon values for Cs, Pb, Sn, Br, and I reproduced in Table S1 (Supporting Information).^[38,39] Simulation models were assembled with the commercial program CrystallMaker from DFT models produced as described and nanotubes generated with the software TubeGen Online version 3.4.^[60]

DFT Technical Details: Density-functional theory (DFT) calculations were performed within the generalized-gradient, Perdew–Burke–Ernzerhof^[61] approximation as implemented in Quantum ESPRESSO.^[62] Structural relaxations employed ultrasoft, scalar-relativistic pseudopotentials,^[63] with fully relativistic pseudopotentials used for band structure calculations (pslibrary 1.0.0^[64]). The pseudopotentials are listed in Table S2 (Supporting Information). Wavefunctions and charge densities were expanded in a plane-wave basis up to energy cutoffs of 60 and 800 Ry, respectively. The 1D structures were relaxed initially in the absence of the nanotube, aligned along the *c* axis in a tetragonal simulation cell, with the *a* parameter fixed to ensure at least 1 nm of vacuum separating periodic replicas. Reciprocal space sampling along the *c* axis ensured a maximum 1.4 nm⁻¹ spacing between *k*-points. Structures were relaxed until forces and pressures fell below 26 meV Å⁻¹ and 0.5 kbar, respectively. A neutralizing jellium background was included for structures with a net charge but no further correction scheme was applied. The relaxed simulation cell parameters and reciprocal space sampling points ($1 \times 1 \times N_{kz}$) are listed in Table S3 (Supporting Information). Γ -point phonons were calculated using the finite displacement method^[65] to check that all frequencies were non-imaginary. The band structures of the models presented in Figure 5 were also recalculated using the PBE0 hybrid functional^[66] at the scalar relativistic level, using the PBE-optimized geometry (see Table S5 and Figure S13, Supporting Information).

Modelling Nanotube Encapsulation: Selected structures were placed inside nanotubes and re-relaxed, sampling reciprocal space at the Γ -point. Carbon nanotubes (CNTs) were constructed based on a lattice parameter of 2.465 Å (C-C bond length 1.4235 Å) that was obtained from a relaxation of graphene (PBE functional, $40 \times 40 \times 1$ *k*-point sampling, 23 Å vacuum spacing). Selected vacuum-relaxed ABX structures were placed in the centre of zigzag or armchair CNTs. The chiral indices of the CNTs were chosen in order to have nanotube radii consistent with the microscopy images and also to minimize the strain placed on the ABX structures due to the lattice matching. Tetragonal simulation cells were used. For (*n,n*) (armchair) nanotubes, $a = 18.521$ Å and $c = N \times 2.465$ Å, and for the (*m,0*) (zigzag) nanotubes $a = 21.167$ Å and $c = N \times 3d_{cc}$, where *N* denotes the number of CNT repeats. The parameters used to construct the simulations are given in Table S4 (Supporting Information). The relaxations inside CNTs confirmed that the structures did not undergo significant changes in the presence of the nanotube. However, due to the introduction of strain, the lower *k*-point sampling and the absence of a phonon analysis, we used the vacuum-relaxed structures when comparing to the experimental images in the TDS STEM simulations. Furthermore, no dispersion corrections were employed in the current calculations. Test calculations on the CsPbBr₃ bilayer using the correction scheme in ref. [67] found no significant changes to the bond lengths and angles and a small lateral displacement of the entire structure within the nanotube. Given the novelty of these structures, further testing of different dispersion correction schemes is required in order to determine which scheme can provide the most reliable and accurate description.^[68]

Supporting Information

Supporting Information is available from the Wiley Online Library or from the author.

Acknowledgements

R.J.K., J.S., R.I.W., and C.E.P. conceived the project. R.J.K. performed the synthesis and aberration corrected transmission electron microscopy characterization of filled nanotube samples with simulations, image processing, structural modelling and structure analysis being carried out by J.S., C.E.P., and R.I.W. HAADF imaging and atomically resolved EELS mapping was performed by Q.M.R. in Daresbury. Theoretical studies were performed by C.E.P. in Oxford. J.S., R.I.W., R.J.K., and C.E.P. wrote the manuscript. Figures were prepared by J.S., C.E.P., Q.M.R., and R.J.K. All authors discussed the results and commented on the manuscript. J.S. and R.J.K. are indebted to the EPSRC (UK) for support from grant EP/R019428/1. C.E.P. is indebted to support from the Royal Society (UK) from grant RGS\R1\201151. The SuperSTEM Laboratory is the UK National Facility for Aberration-Corrected STEM, supported by the EPSRC. Electron microscopy at Warwick is supported by the University of Warwick's Research Technology Platforms.

Conflict of Interest

The authors declare no conflict of interest.

Data Availability Statement

Data used in this work are available via the Warwick data repository at wrap.warwick.ac.uk/172233.

Keywords

carbon nanotubes, density functional theory, electron microscopy, halide perovskites, nanowires, picoscale materials

Received: September 18, 2022

Revised: November 24, 2022

Published online: January 25, 2023

- [1] R. J. D. Tilley, *Perovskites: Structure-Property Relationships*, Wiley, Chichester, UK 2016.
- [2] R. E. Cohen, *Nature* **1992**, 358, 136.
- [3] T. Zheng, J. Wu, D. Xiao, J. Zhu, *Prog. Mater. Sci.* **2018**, 98, 552.
- [4] J. G. Bednorz, K. A. Müller, *Rev. Mod. Phys.* **1988**, 60, 585.
- [5] W. Wang, M. Xiu, X. Xu, W. Zhou, Z. Shao, *Angew. Chem., Int. Ed.* **2020**, 59, 136.
- [6] D. B. Mitzi, C. A. Feild, W. T. Harrison, A. M. Guloy, *Nature* **1994**, 369, 467.
- [7] N. Mercier, *Angew. Chem., Int. Ed.* **2019**, 58, 17912.
- [8] R. L. Milot, G. E. Eperon, H. J. Snaith, M. B. Johnston, L. M. Herz, *Adv. Funct. Mater.* **2015**, 25, 6218.
- [9] M. Sakata, T. Nishiwaki, J. Harada, *J. Phys. Soc. Jap.* **1979**, 47, 232.
- [10] H. Xie, S. Hao, J. Bao, T. J. Slade, J. Snyder, C. Wolverton, M. Kanatzidis, *J. Am. Chem. Soc.* **2020**, 142, 9553.
- [11] J. S. Manser, J. A. Christians, P. V. Kamat, *Chem. Rev.* **2016**, 116, 12956.
- [12] K. P. Marshall, M. Walker, R. I. Walton, R. A. Hatton, *Nat. Energy* **2016**, 1, 16178.
- [13] I. Chung, B. Lee, J. He, R. P. Chang, M. G. Kanatzidis, *Nature* **2012**, 485, 486.
- [14] J. Y. Kim, J.-W. Lee, H. S. Jung, H. Shin, N.-G. Park, *Chem. Rev.* **2020**, 120, 7867.
- [15] J. Mizukashi, K. Arai, K. Fueki, *Sol. Stat. Ion.* **1983**, 11, 203.
- [16] R. Kumar, M. Bag, *Energy Tech* **2021**, 10, 2100889.

- [17] L. Zhang, J. Miao, Q. Li, *Adv. Funct. Mater.* **2020**, *20*, 2003653.
- [18] Q. Li, Z. Chen, I. Tranca, S. Gaastra-Bede, D. Smeulders, S. Tao, *Appl. Surf. Sci.* **2021**, *538*, 148058.
- [19] K. Yamada, S. Funabiki, H. Horimoto, T. Matsui, T. Okuda, S. Ichiba, *Chem. Lett.* **1991**, *20*, 801.
- [20] D. B. Straus, S. Guo, A. M. M. Abeykoon, R. J. Cava, *Adv. Mater.* **2020**, *32*, 2001069.
- [21] J. Siekmann, S. Ravishankar, T. Kirchartz, *ACS Energy Lett.* **2021**, *6*, 3244.
- [22] M. C. Weldman, A. J. Goodman, W. A. Tisdale, *Chem. Mater.* **2017**, *29*, 5019.
- [23] M. Mao, C. C. Stoumpos, M. G. Kanatzidis, *J. Am. Chem. Soc.* **2019**, *141*, 1171.
- [24] P. Cottingham, R. L. Brutchey, *Chem. Mater.* **2018**, *30*, 6711.
- [25] J. Yin, P. Murty, M. De Bastini, I. Dursun, O. Bakr, J.-L. Brédas, O. F. Mohammed, *Sci. Adv.* **2017**, *3*, e1701793.
- [26] D. Bi, X. Li, J. V. Milić, D. J. Kubicki, N. Pellet, J. Luo, T. LaGrange, P. Mettraux, L. Emsley, S. M. Zakeeruddin, M. Grätzel, *Nat. Commun.* **2018**, *9*, 4482.
- [27] M. R. Filip, G. E. Eperon, H. J. Snaith, F. Giustino, *Nat. Commun.* **2014**, *5*, 5757.
- [28] S. Iijima, T. Ichihashi, *Nature* **1993**, *363*, 603.
- [29] F. Yang, M. Wang, D. Q. Zhang, J. Yang, M. Zheng, Y. Li, *Chem. Rev.* **2020**, *120*, 2693.
- [30] J. Sloan, A. I. Kirkland, J. L. Hutchison, M. L. H. Green, *Chem. Commun.* **2002**, 1319.
- [31] R. Senga, H.-P. Komsa, Z. Liu, K. Hirose-Takai, A. V. Krasheninnikov, K. Suenaga, *Nat. Mater.* **2014**, *13*, 1050.
- [32] R. J. Kashtiban, M. G. Burdanova, A. Vasylenko, J. Wynn, P. V. C. Medeiros, Q. Ramasse, A. J. Morris, D. Quigley, J. Lloyd-Hughes, J. Sloan, *ACS Nano* **2011**, *15*, 13389.
- [33] P. V. C. Medeiros, S. R. Marks, J. M. Wynn, A. Vasylenko, Q. Ramasse, D. Quigley, J. Sloan, A. J. Morris, *ACS Nano* **2017**, *11*, 6178.
- [34] E. Philip, J. Sloan, A. I. Kirkland, R. R. Meyer, S. Friedrichs, J. L. Hutchison, M. L. H. Green, *Nat. Mater.* **2003**, *2*, 788.
- [35] A. N. Khlobystov, D. A. Britz, G. A. D. Briggs, *Accts Chem. Res.* **2005**, *38*, 901.
- [36] M. V. Kharlamova, C. Kramberger, P. Rudatis, T. Pichler, D. Eder, *Appl. Phys. A* **2019**, *125*, 320.
- [37] D. A. Muller, B. Edwards, E. J. Kirkland, J. Silcox, *Ultramicroscopy* **2001**, *86*, 371.
- [38] C. A. López, C. Abia, M. C. Alvarez-Galván, B.-K. Hong, M. V. Martínez-Huerta, F. Serrano-Sánchez, F. Carrascoso, A. Castellanos-Gómez, M. T. Fernández-Díaz, J. A. Alonso, *ACS Omega* **2020**, *5*, 5931.
- [39] I. Chung, J.-H. Song, J. Im, J. Androulakis, C. D. Malliaka, H. Li, A. J. Freeman, J. T. Kenney, M. G. Kanatzidis, *J. Am. Chem. Soc.* **2012**, *134*, 8579.
- [40] H. Wu, J. Pi, D. Zhou, Q. Wang, Z. Long, J. Qiu, *Ceram. Int.* **2022**, *48*, 3383.
- [41] J. V. Alemán, A. V. Chadwick, J. He, M. Hess, K. Horie, R. G. Jones, P. Kratochvíl, I. Meisel, I. Mita, G. Moad, S. Penczek, R. F. T. Stepto, *Pure Appl. Chem.* **2007**, *79*, 1801.
- [42] K.-H. Wang, L. Wu, H.-B. Yao, H.-S. Qian, S.-H. Yu, *Angew. Chem., Int. Ed.* **2016**, *55*, 8328.
- [43] L.-Y. Huang, W. R. L. Lambrecht, *Phys. Rev. B* **2013**, *88*, 165203.
- [44] J. Wiktor, U. Rothlisberger, A. J. Pasquarello, *J. Phys. Chem. Lett.* **2017**, *8*, 5507.
- [45] G. Di Liberto, O. Fatale, G. Pacchione, *Phys. Chem. Chem. Phys.* **2021**, *23*, 3031.
- [46] L. A. Cipriano, G. Liberto, S. Tosoni, G. Pacchione, *Nanoscale* **2020**, *12*, 17494.
- [47] H. Yu, R. A. Loomis, L.-W. Wang, W. E. Buhro, *Nat. Mater.* **2003**, *2*, 517.
- [48] H.-P. Komsa, R. Senga, K. Suenaga, A. V. Krasheninnikov, *Nano Lett.* **2017**, *17*, 3694.
- [49] J. Xue, R. Wang, Y. Yang, *Nat. Rev. Mater.* **2020**, *5*, 809.
- [50] C. Motta, F. El-Mellouhi, S. Sanvito, *Sci. Rep.* **2015**, *5*, 12746.
- [51] R. Prasanna, A. Gold-Parker, T. Leijtens, B. Conings, A. Babayigit, H.-G. Boyen, M. F. Toney, M. D. McGehee, *J. Am. Chem. Soc.* **2017**, *139*, 11117.
- [52] R. B. Weisman, S. M. Bachilo, *Nano Lett.* **2003**, *3*, 1235.
- [53] W.-Q. Han, C. W. Chang, A. Zettl, *Nano Lett.* **2004**, *4*, 1355.
- [54] E. A. Anumol, A. M. Enyashin, N. M. Batra, P. M. F. J. Costa, F. L. Deepak, *Nanoscale* **2016**, *8*, 12170.
- [55] A. N. Enyashin, G. Seifert, *Chem. Phys. Lett.* **2010**, *501*, 98.
- [56] D. B. Straus, R. J. Cava, *ACS Appl. Mater. Interfaces* **2022**, *14*, 34884.
- [57] A. M. Ulatowski, A. D. Wright, B. Wenger, L. R. V. Buizza, S. G. Motti, H. J. Eggimann, K. J. Savill, J. Borchert, H. J. Snaith, M. B. Johnston, L. M. Herz, *J. Phys. Chem. Lett.* **2020**, *11*, 3681.
- [58] J. Sloan, D. M. Wright, H.-G. Woo, S. Bailey, G. Brown, A. P. E. York, K. S. Coleman, J. L. Hutchison, M. L. H. Green, *Chem. Commun.* **1999**, 699.
- [59] J. J. Peters, M. A. Dyson, OpenCL accelerated multislice simulation for electron microscopy, <https://github.com/JJPeters/cITEM/tree/v0.3.3a> (accessed: December 2022).
- [60] J. T. Frey, D. J. Doren, TubeGen Online – Version 3.4 <https://turin.nss.udel.edu/research/tubegenonline.html> (accessed: December 2022).
- [61] J. P. Perdew, K. Burke, M. Ernzerhof, *Phys. Rev. Lett.* **1996**, *77*, 3865.
- [62] P. Giannozzi, S. Baroni, N. Bonini, M. Calandra, R. Car, C. Cavazzoni, D. Ceresoli, G. L. Chiarotti, M. Cococcioni, I. Dabo, A. Dal Corso, S. de Gironcoli, S. Fabris, G. Fratesi, R. Gebauer, U. Gerstmann, C. Gougoussis, A. Kokalj, M. Lazzeri, L. Martin-Samos, N. Marzari, F. Mauri, R. Mazzarello, S. Paolini, A. Pasquarello, L. Paulatto, C. Sbraccia, S. Scandolo, G. Sclauzero, A. P. Seitsonen, et al., *J. Phys.: Condens. Matter* **2009**, *21*, 395502.
- [63] D. Vanderbilt, *Phys. Rev. B* **1990**, *41*, 7892.
- [64] A. Dal Corso, *Comp. Mater. Sci.* **2014**, *95*, 337.
- [65] G. J. Ackland, M. C. Warren, S. J. Clark, *J. Phys.: Condens. Matter* **1997**, *9*, 7861.
- [66] C. Adamo, V. Barone, *J. Chem. Phys.* **1999**, *110*, 6158.
- [67] S. Grimme, *J. Comp. Chem.* **2006**, *27*, 1787.
- [68] M. Stöhr, T. Van Voorhis, A. Tkatchenko, *Chem. Soc. Rev.* **2019**, *48*, 4118.